nature communications

Article

https://doi.org/10.1038/s41467-025-62892-7

Conductivity hysteresis in MXene driven by structural dynamics of nanoconfined water

Received: 27 January 2025

Accepted: 31 July 2025

Published online: 12 August 2025

Check for updates

Teng Zhang[1,8], Katherine A. Mazzio[2,3,8], Ruocun John Wang[1,4,8], Mailis Lounasvuori[3], Ameer Al-Temimy[3], Faidra Amargianou[3], Mohamad-Assaad Mawass[3,7], Florian Kronast[3], Daniel M. Többens[3], Klaus Lips[3,5,6], Tristan Petit[3] ✉ & Yury Gogotsi[1] ✉

Water under 2D confinement exhibits unique structural and dynamic behaviors distinct from bulk water, including phase transitions and altered hydrogen-bonding networks, making it of great scientific interest. While confinement in 2D materials like graphene, mica, or hexagonal boron nitride has been reported, their lack of intrinsic hydrophilicity or metallic conductivity limits their suitability for probing the interplay between confined water and electronic transport. MXenes, a family of 2D transition metal carbides and nitrides, overcome these limitations by combining high metallic conductivity (~10^4 S cm^{-1}) with hydrophilicity, offering a unique platform to investigate confined water dynamics and their influence on electronic properties. Here, we show that temperature and confinement drive structural transitions of water within MXene interlayers, including the formation of localized ice clusters, amorphous ice, and dynamic hydrogen-bonded networks. These transformations disrupt stacking order, inducing a reversible metal-to-semiconductor transition and conductivity hysteresis in MXene films. Upon heating to 340 K, the dissociation of ice clusters restores interlayer spacing and metallic behavior. Our findings experimentally establish MXenes as an exceptional platform for studying the phase change of confined water, offering new insights into how nanoscale water dynamics modulate electronic properties and enabling the design of advanced devices with tunable interlayer interactions.

Water is fundamental for a wide range of physical, chemical, and geological processes[1–5]. Water confined within nanoscale spaces has attracted substantial attention in recent years, as it exhibits unique behaviors and properties different from bulk water[6–11]. The properties of confined water are governed by the confinement dimensions, morphology, material surface properties, and the presence of solvated ions or molecules[4,12]. Despite advances in nanoscale characterization tools and molecular dynamics simulations, achieving comprehensive insight into confined water properties remains challenging[13–16].

Previous research has shown that water confined in low-dimensional materials has different phase transition temperatures, transport, and dielectric properties. For instance, water confined within hydrophobic slits exhibits a low phase transition temperature, and water confined between graphene or MXene sheets exhibits low or

[1]A.J. Drexel Nanomaterials Institute and Department of Materials Science and Engineering, Drexel University, Philadelphia, PA, USA. [2]Department of Chemistry, Humboldt University of Berlin, Berlin, Germany. [3]Helmholtz-Zentrum Berlin für Materialien und Energie GmbH, Berlin, Germany. [4]Department of Materials Science and Engineering, University of North Texas, Denton, TX, USA. [5]Department of Physics, Freie Universität Berlin, Berlin, Germany. [6]Department of Physics and Astronomy, University of Utah, Salt Lake City, USA. [7]Present address: Department of Interface Science, Fritz Haber Institute of the Max Planck Society, Berlin, Germany. [8]These authors contributed equally: Teng Zhang, Katherine A. Mazzio, Ruocun John Wang. ✉e-mail: tristan.petit@helmholtz-berlin.de; gogotsi@drexel.edu

even negative dielectric constants[6,8,17,18]. These properties of nanoconfined water are important in energy storage, sensing, catalysis, drug delivery, and other technologies[3,19–22]. For example, in energy storage, nanoconfined water was found to promote the transport of ions and dampen the interaction between intercalants and host materials, leading to pseudocapacitive charge storage[23,24]. However, despite the numerous studies on the properties and applications of nanoconfined water, the electronic conductivity of confined water remains largely unexplored. In single-walled carbon nanotube (SWCNT) mats, a small dose of water was found to improve their electrical conductivity[25,26]. This phenomenon was attributed to either an improved intra-tube conductivity due to water doping or an improved inter-tube conductivity due to momentum resonance achieved by adsorbed water molecules[25,26]. However, the significance of inter- versus intra-tube conductance is not clear. The role of intercalated ions on the transport properties of confined water has been studied, but is still poorly understood[27–30]. In many materials, nanoconfined water contains ions to balance the charge of the adjacent surfaces. The effect of nanoconfined water on the electronic properties of materials is difficult to investigate because most confining nanomaterials are either dielectric (clay, graphene oxide, BN, etc.) or hydrophobic (graphene)[4].

2D carbides and nitrides of transition metals known as MXenes offer a unique platform for studying water under 2D confinement due to their high hydrophilicity and small interlayer spacing. Figure 1 shows $Ti_3C_2T_x$ MXene, where T_x stands for surface functional groups including −O−, −OH, −F, and −Cl. Among these, the −OH/−O− surface groups provide a hydrophilic surface, readily forming hydrogen bonds with water molecules. This hydrophilicity drives water into the interlayer spaces of restacked MXenes, typically forming one to three layers of nanoconfined water depending on humidity and temperature[31,32]. This has the impact of allowing stable water adsorption in significantly narrower slits due to hydrogen bonding interactions, in contrast to water confinement between hydrophobic layers, such as graphene, which rely on weak van der Waals interactions[33]. Metallic materials, including MXenes, usually show a positive temperature coefficient of resistance ($d\rho/dT > 0$) due to increased atomic and free electron movement with temperature, resulting in a larger number of collisions and, therefore, energy loss. However, deviations from this behavior have been observed in MXenes and are most likely attributed to interactions with confined water and intercalated ions within the layers. The intercalated cations exhibit distinct affinity for water molecules and the MXene surface, which influences the structure of the confined water. Molecular dynamics simulations indicate that Li^+ and Na^+ ions prefer to stay close to the MXene surface, while K^+ ions reside in the middle of the water network[34]. In contrast, under acidic media, hydronium formation extracts water molecules from MXene layers, making MXene interlayers with little to no confined water[35]. By selectively intercalating Li^+, Na^+, K^+, and H^+ ions, we can manipulate the structure of confined water between MXene layers (Fig. 1a)[36]. $Ti_3C_2T_x$ and some other MXenes behave like metallic conductors despite the presence of one to three layers of nanoconfined water between the MXene sheets[37]. Nonetheless, the amount of interlayer water affects the electronic conductivity of MXene thin films. For instance, the co-intercalation of water during electrochemical protonation was found to correlate directly with the in-plane conductivity of MXenes, potentially through changing the interlayer spacing[38]. This active modulation of the electronic conductivity has already been applied to dynamically adjust the electromagnetic interference shielding properties of MXene[39]. These initial studies of MXene structures and confined water-ion interactions point to the importance of understanding the interplay between confined water and the electronic properties of MXene thin films. However, the role of MXene flake ordering on the electronic structure remains unclear.

In this work, we study the effect of ion solvation and temperature on the electronic conductivity of MXenes with nanoconfined water through resistivity measurements, synchrotron X-ray diffraction (XRD), X-ray Photoemission Electron Microscopy (XPEEM), and differential scanning calorimetry (DSC) near the nominal freezing point of water (200 K to 380 K). We demonstrate unusual hysteresis of the resistivity and positive to negative $d\rho/dT$ transitions as a function of temperature for MXene systems containing alkali ions and confined water. The hydrogen bonding of confined water molecules and their spatial distribution over the MXene film were probed using XPEEM. We observed various degrees of MXene interlayer spacing change upon thermal cycling due to different ions. Still, we did not detect any crystalline ice phases reported for other 2D materials, only an amorphous ice phase. These findings provide fundamentally new insights into water-ion interactions under 2D confinement.

Result and discussion

Electronic transport properties of MXene with confined water

We measured the resistivity of $Ti_3C_2T_x$ thin films intercalated with Li^+, Na^+, K^+, and H^+ (noted as Li-$Ti_3C_2T_x$, Na-$Ti_3C_2T_x$, K-$Ti_3C_2T_x$, and H-$Ti_3C_2T_x$) using four-point-probe resistivity measurements during continuous thermal cycling between 300 K and 200 K under vacuum. A temperature-dependent hysteresis was observed (Fig. 2a). To monitor structural changes, thermal cycling was repeated several times, and the hysteresis was found to expand and stabilize by the third cycle for all samples. Therefore, we focused our detailed analysis on the third thermal cycle.

The resistivity of the H-$Ti_3C_2T_x$ thin film exhibited metallic behavior ($d\rho/dT > 0$) throughout the thermal cycle, as expected for metallic MXenes[35]. Despite the difference in intercalants, all $Ti_3C_2T_x$ thin films displayed similar $d\rho/dT$ behavior in the metallic region (~200–240 K), indicating this is an intrinsic property of $Ti_3C_2T_x$ MXene. However, for Li^+, Na^+, and K^+ intercalated $Ti_3C_2T_x$ films, a semiconductor-like behavior ($d\rho/dT < 0$) emerged during both cooling and heating cycles at

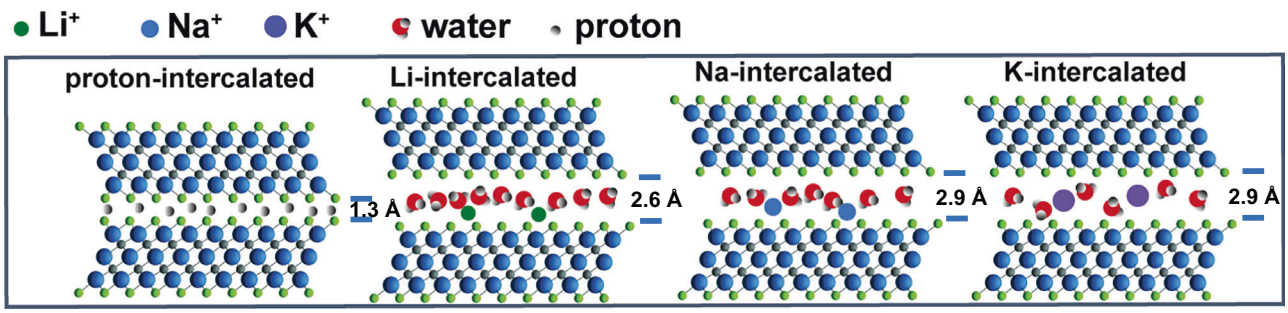

Fig. 1 | Schematic illustration of the interaction between confined water, intercalated ions, and MXene. Protons and other cations are intercalated between the MXene sheets with one layer of confined water. MXene with Li^+ intercalation has the most water molecules confined in the interlayer, followed by Na^+ and K^+. Note that protons eliminate the water layer after drying.

https://doi.org/10.1038/s41467-025-62892-7

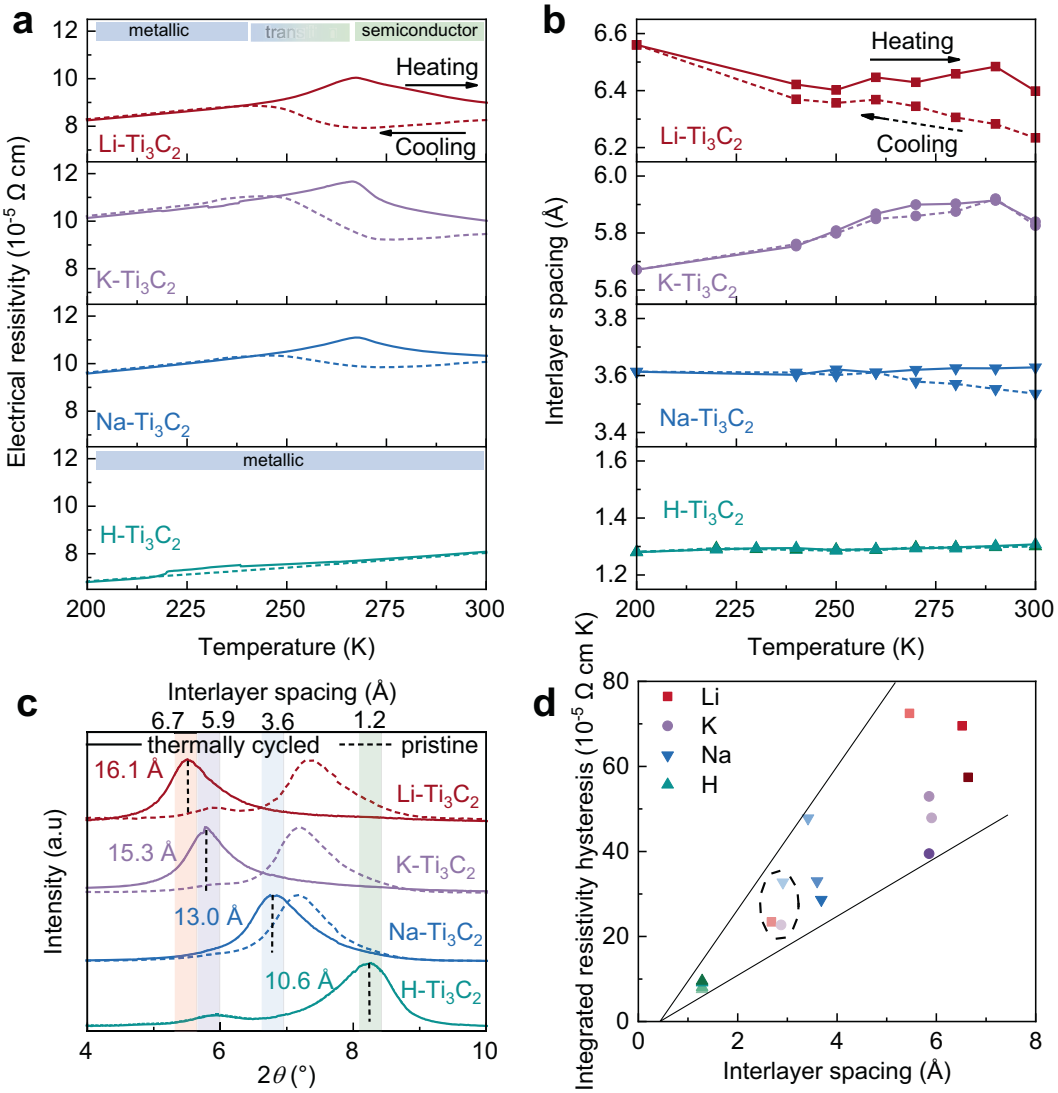

Fig. 2 | Temperature dependence of electrical resistivity and interlayer spacing of MXene films with Li^+, Na^+, K^+, and H^+ intercalants, noted as Li-Ti_3C_2, Na-Ti_3C_2, K-Ti_3C_2, and H-Ti_3C_2. a Electrical resistivity of MXenes as a function of temperature during the third thermal cycle. **b** Interlayer spacing before and after the third cooling-heating cycle. **c** 002 reflections of pristine MXenes and after the third cooling-heating cycles of the MXenes at 300 K. **d** Integrated resistivity hysteresis for ion-intercalated $Ti_3C_2T_x$ samples and their corresponding interlayer spacing at 300 K for all thermal cycles. The circled (dashed line) points are MXenes from the first thermal cycle. The color darkness of the points increases with the number of cycles, and the errors are within the order of the size of the symbols.

higher temperatures. This semiconductor-like transition appeared between ~273–245 K during cooling and 245–267 K during heating. Notably, this transition temperature region during thermal cycling is significantly below the freezing point of bulk water, suggesting it was related to a structural transition of the confined water in the MXene interlayers, where the freezing point of water can be suppressed[40,41]. After heat treatment at 353 K at high vacuum over 12 h, which is expected to remove nearly all physiosorbed water from the interlayer confinement, the Li-$Ti_3C_2T_x$ film subsequently shows pure metallic behavior during cooling and heating cycles (Supplementary Fig. S1), reinforcing the hypothesis that confined water plays a crucial role in the observed transition[37,42].

Structural changes during thermal cycling

To probe any structural changes, we performed in-situ XRD measurements on cation-intercalated MXene films during three heating/cooling cycles between 300 K and 200 K under a helium atmosphere. Figure 2b presents the XRD patterns in the 002 peak region for all MXene samples at 300 K before cycling and after the third thermal cycle (XRD patterns over a broader range are shown in Supplementary Figs. S2–S5). Considering a monolayer thickness of the $Ti_3C_2T_x$ of 9.4 Å, the interlayer spacings could be calculated from the 002 reflections and were determined to be 2.6 Å, 2.9 Å, and 2.9 Å for pristine Li^+, Na^+, and K^+ intercalated $Ti_3C_2T_x$ before thermal cycling, respectively—corresponding to one layer of confined water[43]. In contrast, the H^+ intercalated MXene exhibited a significantly smaller interlayer spacing of 1.25 Å, close to the size of the hydronium ion (1.02 Å)[44]. A possible explanation is that the strong interactions between hydronium ions and the oxygen-terminated MXene surface cause contraction of the interlayers and expulsion of water in acidic media. In such conditions, protons/hydronium ions (H_3O^+) intercalate and interact strongly with the MXene surface terminations (predominantly –O sites)[36,45]. This process leads to observable changes in the surface chemistry, such as an increase in –OH terminations, and results in a significantly reduced amount of confined

https://doi.org/10.1038/s41467-025-62892-7

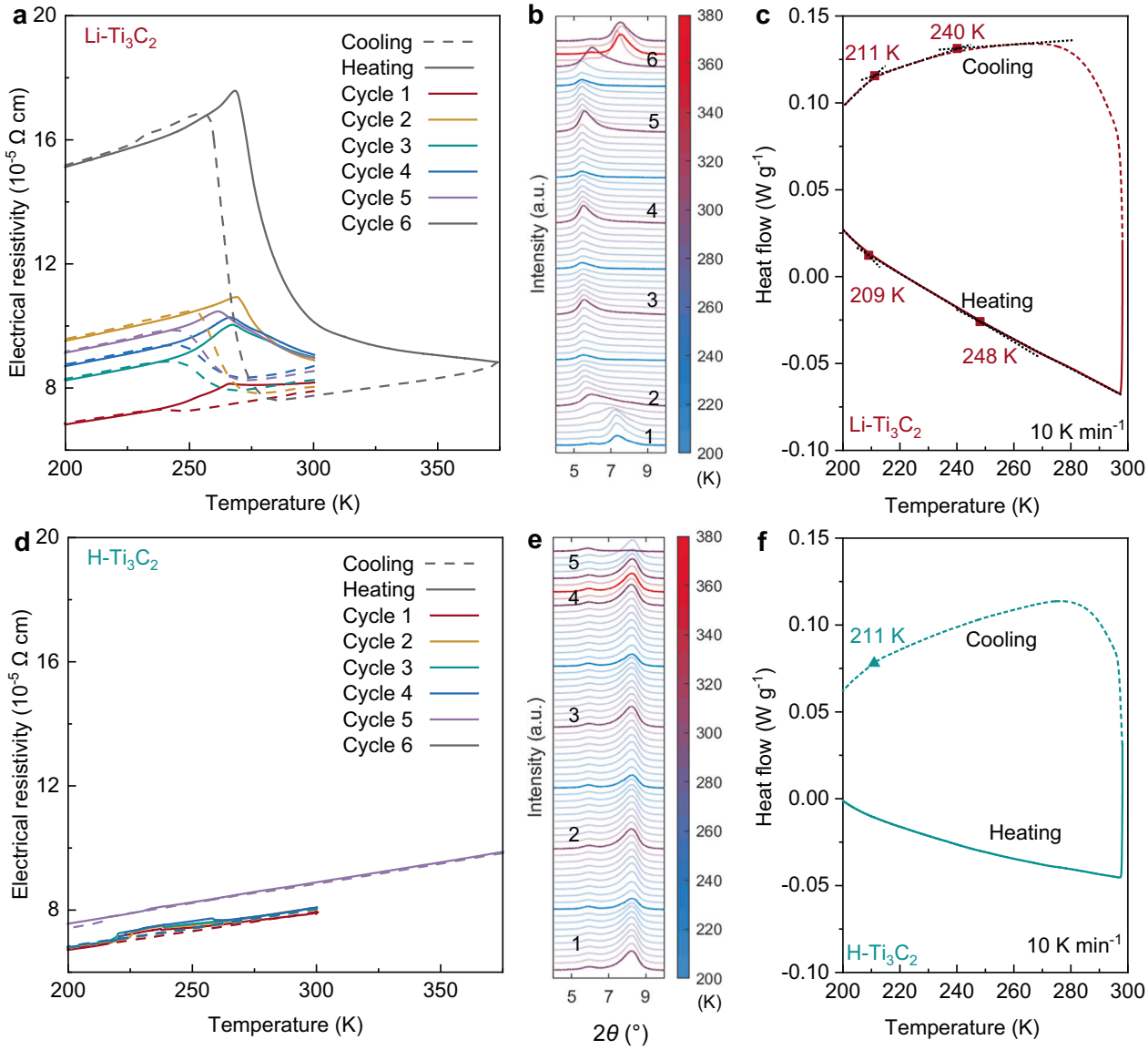

Fig. 3 | Role of confined water within MXene interlayer on thermal hysteresis during heating/cooling cycles. Thermal hysteresis of electrical resistivity of (**a**) Li-$Ti_3C_2T_x$ MXene and (**d**) H-$Ti_3C_2T_x$ MXene between 200 K and 300 K in the first five thermal cycles followed by heating to 375 K and beginning the fifth thermal cycle with cooling and heating between 400 K and 200 K, at $dT/dt = 3$ K min^{-1}. Cycle 6 began with cooling from 375 K to 200 K, followed by reheating to 380 K. The same legend of cycles is shared by (**a**, **d**). X-ray Diffraction (XRD) patterns of (**b**) Li-$Ti_3C_2T_x$ and (**e**) H-$Ti_3C_2T_x$ MXene between 200 K and 300 K at repeating thermal cycles followed by heating to 380 K and cooling back to 300 K. **c**, **f** Differential scanning calorimetry (DSC) study of **a** Li-$Ti_3C_2T_x$ MXene and **b** H-$Ti_3C_2T_x$ MXene between 200 K and 300 K recorded at $dT/dt = 10$ K min^{-1}.

water compared to alkali ion intercalated samples. This dehydration effect upon protonation/acid treatment is confirmed by the thermogravimetric analysis (TGA) and X-ray photoelectron spectroscopy (XPS) (Supplementary Figs. S6–S9), which show the lowest water content and the highest –OH fraction in the H-$Ti_3C_2T_x$ sample, consistent with previous vibrational spectroscopy studies[36,45]. The resulting water-depleted state of H-$Ti_3C_2T_x$ serves as an essential control in our study, highlighting the role of confined water in the temperature-dependent electronic behavior observed in the other samples.

After the third thermal cycle, the interlayer spacing expanded to 6.7 Å, 3.6 Å, and 5.9 Å for Li^+, Na^+, and K^+ intercalated MXenes, respectively (Fig. 2c). These expanded interlayer spacings remained stable during subsequent thermal cycles (Supplementary Fig. S10, S12, S13). In contrast, the H^+ intercalated MXene maintained a consistent interlayer spacing of ~1.3 Å across all cycles, likely due to the absence of confined water (Supplementary Fig. S11). The interlayer expansion observed during thermal cycling was, therefore, likely associated with the rearrangement of the confined water molecules or changes in the solvation structure around the intercalated ions.

The magnitude of resistivity changes and thermal hysteresis correlated with the interlayer spacing. We quantified the thermal hysteresis by integrating the area enclosed by the resistivity–temperature curves (Fig. 2d). Minimal thermal hysteresis was observed in the H^+ intercalated MXene, which showed consistent interlayer spacing across all thermal cycles. In contrast, the Li^+, Na^+, and K^+ intercalated MXenes displayed the smallest hysteresis during the first thermal cycle (highlighted by the dashed circle in Fig. 2d), with hysteresis increasing after the first cycle. The interlayer spacing expanded further after the first cycle in the order: $Li^+ > K^+ > Na^+ > H^+$ intercalated MXenes, accompanied by an increase in integrated hysteresis.

Validation of the critical role of confined water

We validated the critical role of confined water on the temperature-dependent resistivity by comparing the thermal hysteresis in H^+ and Li^+ intercalated $Ti_3C_2T_x$ MXenes (Fig. 3). During the initial thermal cycling, Li-$Ti_3C_2T_x$ showed a minimum thermal hysteresis (Fig. 3a). Upon cooling from 300 K to 200 K, it showed metallic-like behavior with a positive temperature coefficient of resistivity ($d\rho/dT = 0.0120\ \Omega\ cm\ K^{-1}$). A minor semiconductor-like behavior ($d\rho/dT = -0.0038\ \Omega\ cm\ K^{-1}$) emerged between 248 K and 240 K. During heating from 200 K, metallic behavior ($d\rho/dT = 0.0114\ \Omega\ cm\ K^{-1}$) persisted up to 243 K. Between 243 K and 266 K, the $d\rho/dT$ slope doubled, and beyond 266 K, a semiconductor-like behavior ($d\rho/dT = -0.0051\ \Omega\ cm\ K^{-1}$) reappeared, transitioning back to metallic behavior at temperatures above 275 K.

To gain insights into structural changes during thermal cycling, we conducted in-situ XRD measurements on the Li-$Ti_3C_2T_x$ (Fig. 3b and Supplementary Fig. S2). At 300 K before cycling, the 002 peak at 7.3° 2θ indicated an effective monolayer of confined water. As the sample cooled, the 002 peak gradually shifted to 6.0° 2θ with a significant decrease in intensity, suggesting reduced structural ordering and interlayer expansion. The interlayer spacing increased to 5.5 Å during the first thermal cycle, indicating substantial structural changes in the confined water. This interlayer expansion likely contributes to the observed semiconductor-like behavior ($d\rho/dT < 0$) after the first cycle.

Upon heating, the interlayer remained expanded and stabilized with minimal shifts to lower angles during subsequent thermal cycles (Δd < 1 Å, cycles 2–5, Supplementary Fig. S10). Although the 002 peak intensity reached its minimum at 200 K, it recovered upon reheating to 300 K, indicating a partial reordering of the layers. This reversible change in intensity—contrasted with the largely irreversible peak shift—suggests that the MXene sheets undergo continuous rearrangement during repeated thermal cycling. We attribute this behavior to turbostratic disorder, wherein the *c*-axis alignment of stacked layers and their spacing varies without permanently disrupting structural coherence. Such broadened peaks and smeared diffraction are common in restacked 2D materials when the stacked nanosheets are not perfectly aligned[46].

Between cycles 2 and 5, we observed an increase in the resistivity thermal hysteresis, with more pronounced semiconductor-like behavior ($d\rho/dT < 0$) during both heating and cooling (Fig. 3a). The temperature range for semiconductor-like behavior extended from 9 K in the first cycle to 30 K in subsequent cycles, with the transition back to metallic behavior consistently occurring at ~243 K. The magnitude of $d\rho/dT$ in the semiconductor-like range also increased with each cycle (Supplementary Fig. S15).

Similar phenomena were observed in K^+ and Na^+ intercalated $Ti_3C_2T_x$ MXene, both initially containing one layer of confined water before thermal cycling (Supplementary Figs. S12–S14). In contrast, the H-$Ti_3C_2T_x$, with minimal confined water, exhibited no significant changes in resistivity (Fig. 3d) or interlayer spacing (Fig. 3e and Supplementary Fig. S11). Introducing H^+ decreased the interlayer spacing, thus increasing the van der Waals interaction between the MXene layers[35,47]. The higher conductivity of H-$Ti_3C_2T_x$ may also be partly attributed to the intercalated protons facilitating electron transport—a hypothesis that requires further investigation, which is beyond the scope of this study.

To further assess the role of confined water, we annealed the MXene films at 380 K after the fifth thermal cycle (Fig. 3a). Beginning at 340 K and continuing to 380 K, the corresponding XRD patterns showed a shift of the 002 reflection to a higher angle that is slightly higher than the initial position in the pristine sample (Supplementary Fig. S16). This higher temperature heating causes the loss of weakly confined water, further reducing interlayer spacing. Cooling the annealed samples to room temperature (300 K) produced XRD patterns resembling those of the pristine material but with diminished intensity (Supplementary Fig. S17), indicating increased turbostratic disorder due to water loss. This misalignment likely disrupted inter-flake electron transport, significantly contributing to the observed resistivity hysteresis (Supplementary Fig. S14c, cycle 6)[37,48].

Differential scanning calorimetry (DSC) measurements provided additional insights into structural transitions during thermal cycling between 200 K and 300 K (Fig. 3c). During cooling, a slope change in the heat flow at 240 K was observed for Li^+ intercalated MXene, interpreted as the glass transition (T_g) of the nanoconfined water, consistent with calorimetric studies of water in other nanoporous systems[49,50]. This transition aligns closely with the semiconductor-to-metal transition temperature (~243 K) observed in the resistivity measurements. Similar glass transitions at around 240 K were detected for Na^+ and K^+ intercalated MXenes (Supplementary Fig. S18). Importantly, consistent with previous observations, this feature is absent in the H^+ intercalated MXene (Fig. 3f), which contains no or minimal amounts of confined water, implicating confined water as the cause of this transition.

Local chemical bonding of intercalated water molecules during thermal transitions

Building upon our observations of the critical role of confined water in temperature-dependent resistivity and structural changes, we further investigated the local chemical bonding environment of the intercalated water molecules. This was achieved using low-temperature X-ray photoemission electron microscopy (XPEEM) on Li-$Ti_3C_2T_x$ MXene (Fig. 4a). XPEEM is a powerful technique that combines imaging and spectroscopy to provide spatially resolved chemical information at the nanoscale. Imaging at the oxygen K-edge over the 220 K to 300 K temperature range revealed micron-scale surface heterogeneities (Figs. 4b–e) with distinct X-ray absorption spectroscopy (XAS) signatures.

XAS at the oxygen *K*-edge, recorded locally with XPEEM, provided high chemical sensitivity to the MXene oxygen surface terminations and the hydrogen-bonding environment of water within the interlayer galleries. At 220 K, the XA spectrum exhibited pronounced doublet peaks at 531.0 eV and 533.2 eV, corresponding to 3 *d* bonding states of titanium with predominant t_{2g} and e_g symmetries, respectively. At higher temperatures, water-related features emerged in the XA spectra, with components corresponding to short-range (I, 533.3 eV), intermediate-range (II, 535.8 eV), and long-range (III, ~539 eV) hydrogen-bonding order (Fig. 4b)[44]. At 220 K and 240 K, only short- and long-range ordering was observed, corresponding to isolated water molecules and ice clusters in sub-micrometer regions (Fig. 4c)[51,52]. Above 260 K, the spectra evolved markedly, indicating dramatic changes in the water hydrogen-bonding network[53]. The water molecules transition from localized ice clusters to a two-dimensional (2D) confined water layer with intermediate-range ordering, suggesting an amorphous ice structure, consistent with the XRD data showing no crystalline ice reflections[51,52]. At 300 K, the long-range water ordering post-edge (III) appeared, which is associated with double hydrogen-bonded water molecules. This feature has a lower relative intensity compared to liquid water due to the confinement within the MXene interlayer. The enhanced pre-edge feature (I) indicates restricted intermolecular hydrogen bonding, consistent with previous FTIR observations. [45]

The difference spectra shown in Fig. 4d are thus representative of 2D confined water layers. The electronic signature of the confined water within the MXene interlayer at 260 K appears similar to that in porous carbon materials, where no long-range ordering in the hydrogen bonding was detected[54]. In contrast, the longer-range ordering observed at 300 K is not possible in nanopores. It is related to the 2D extended hydrogen-bond network facilitated by hydrogen bonds with the MXene oxygen surface terminations. Although only minor spectral differences were observed between the initial water clusters and the

https://doi.org/10.1038/s41467-025-62892-7

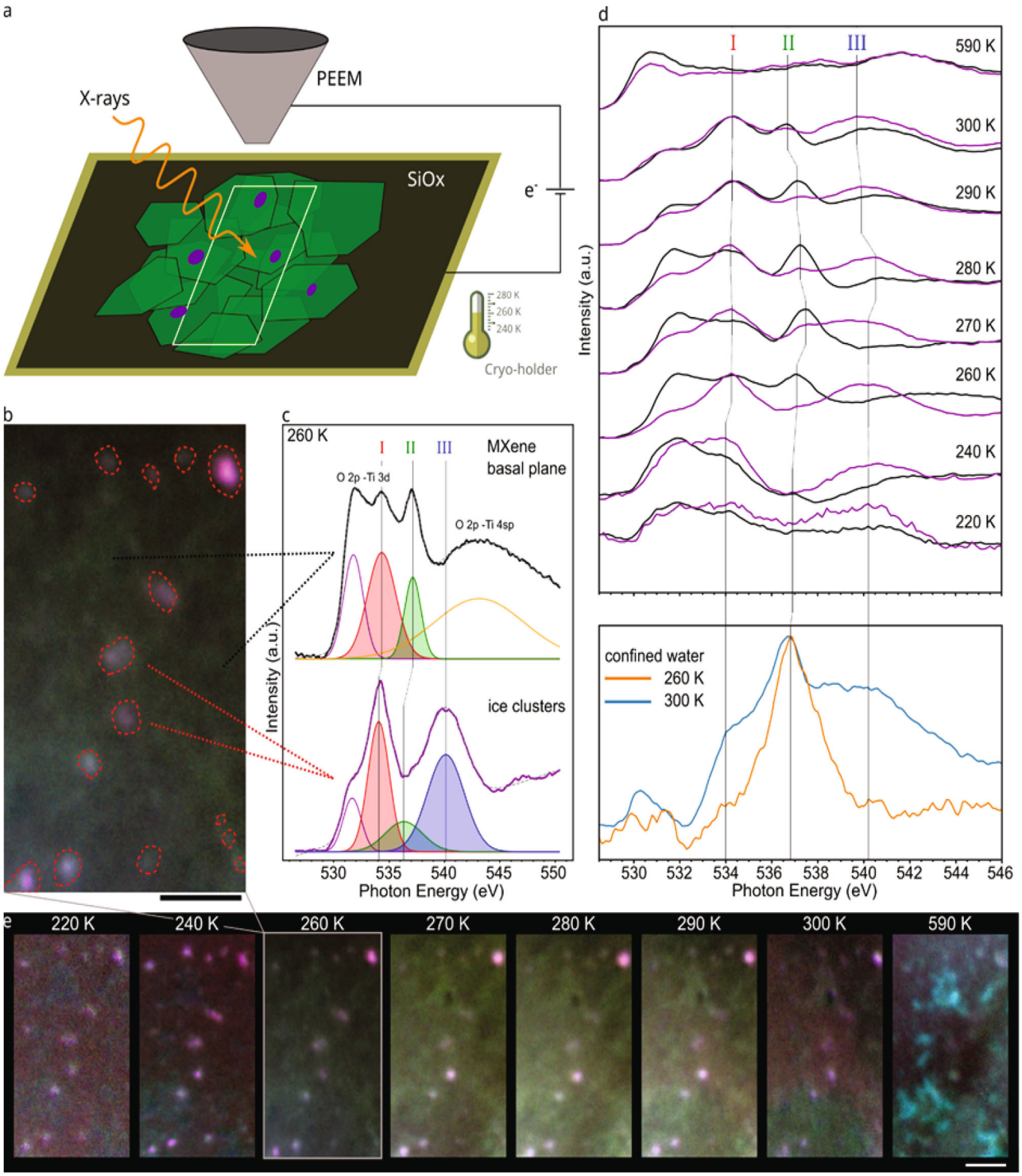

Fig. 4 | Temperature-dependent XPEEM of Li-$Ti_3C_2T_x$ MXene. a Schematic of the in situ X-ray Photoemission Electron Microscopy (XPEEM) imaging upon heating. **b** XPEEM micrographs of a Li-$Ti_3C_2T_x$ film at 260 K. The color scale is based on the respective contribution of the three water bands (I: red, II: green, III: blue) over the MXene film. Ice clusters are circled by dashed red lines. **c** X-ray absorption spectroscopy (XAS) at the oxygen *K*-edge of the MXene film (green region) and ice clusters (purple region) are shown with their peak fitting. **d** Temperature-dependent XAS at the oxygen *K*-edge of the ice clusters (purple) and MXene film (black) between 220 and 590 K. The spectra are normalized and offset vertically for clarity. The XA spectra from confined water are obtained by subtracting the XA spectrum at 240 K from those recorded at 260 K and 300 K. **e** XPEEM micrographs over the 220–590 K temperature series. The scale bars are 2 μm.

rest of the MXene film at 300 K, contrast differences remained visible throughout the film.

After annealing at 590 K, most confined water molecules were desorbed, as evidenced by the disappearance of ice clusters and water-related XAS features. The remaining oxygen signals were attributed to MXene surface terminations rather than confined water, consistent with negligible changes in the Ti *L*-edge spectra (Supplementary Fig. S24). This observation aligns with the DSC and XRD-derived understanding of the MXene thermal response. The microscopic insights into water clustering and phase changes during the metal-

https://doi.org/10.1038/s41467-025-62892-7

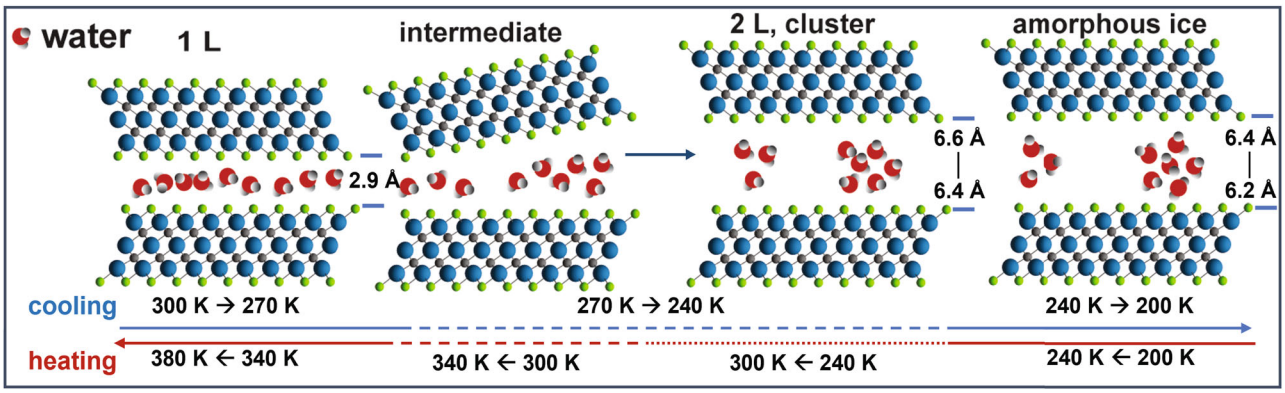

Fig. 5 | Schematic summarizing the proposed temperature-dependent structural transitions of confined water correlated with electronic changes. Based on experimental results, water within MXene interlayers is proposed to transition during cooling (top path) from a quasi-2D liquid-like layer (~300 K) to localized water clusters (~240 K) and an amorphous ice-like state (~200 K). Dissociation of these structures upon heating (bottom path) restores the initial state, with the overall cycle correlating with observed changes in interlayer spacing, stacking order, and electronic conductivity hysteresis.

semiconductor transition provided by XPEEM help interpret the macroscopic glass transitions observed in the resistivity and XRD measurements.

Influence of confined water on resistivity and interlayer spacing

The observed changes in resistivity and interlayer spacing are directly related to the conformational changes of confined water molecules between MXene layers at varying temperatures. At 300 K, the MXene layers are well aligned, as confirmed by the maximum intensity of the 002 peaks in the initial XRD patterns[55]. As the temperature decreases to 270 K, water molecules nucleate and form amorphous ice clusters within the interlayer galleries. This clustering maximizes hydrogen bonding with neighboring water molecules and the MXene surface, as observed by XPEEM, and extends a few hundred nanometers upon further cooling.

The ultra-high lateral pressure between MXene layers with non-uniform surface terminations may explain the absence of hexagonal ice formation[40]. The measured adhesion energy of monolayer $Ti_3C_2T_x$ is approximately 0.90 J m^{-2} [56]. We calculated the van der Waals pressure between MXene with 6 Å interlayer spacing as 1.2–2.5 GPa, which agrees with the first principles study result that the 2D ice can spontaneously form at 250 K in a 6.0 Å nano-slit under high pressure (Table S3)[40]. The reduced dynamics of water molecules and decreased interlayer distance reduce scattering during intra-flake electron hopping, possibly inducing the metallic behavior observed at temperatures below 240 K[57,58].

The transition from liquid-like water to amorphous ice between 300 K and 200 K leads to an expansion of the MXene interlayer spacing, as indicated by the XRD data. As amorphous ice clusters form, a higher temperature is required to break the strong hydrogen bonds between the water molecules and the MXene surface. Additionally, more energy is needed to desorb the water clusters compared to their formation energy[47]. Therefore, heating up to 340 K instead of 300 K is required to disrupt the hydrogen-bonding network of the amorphous ice clusters, as confirmed by the 002 XRD reflections shifting back to their original positions at 340 K (Supplementary Fig. S14)[42,43]. During the heating of Li-$Ti_3C_2T_x$, a glass transition is observed at 248 K (Supplementary Fig. S18). Crucially, MXenes incorporating confined water demonstrate dynamic motion activation near 253 K—a behavior absent in samples without weakly confined water[59]. This observation indicates a transition from a glassy to a more dynamic state within the interlayer regions of MXene, facilitated by the presence of clusters of confined water molecules and a realignment of the MXene layers. The transitions observed at higher temperatures (343 K for Li^+, 331 K for Na^+, and 347 K for K^+ intercalated MXenes) further corroborate the influence of confined water on the structural ordering of MXene (Supplementary Fig. S16). The corresponding XRD peak shifts at approximately 340 K are consistent with these transitions, suggesting a thermally induced reorganization of the interlayer spacing and water molecule configuration (Supplementary Fig. S16). A stacked plot analysis (Supplementary Figs. S19 and S20) delineates the intricate relationship between electrical resistivity (ρ), microstructure, and phase transitions in the MXene/confined water systems. The analysis reveals a two-stage thermal response of the confined water upon heating, as shown schematically in Fig. 5:

1. The initial stage involves transitioning from a glassy amorphous state of ice clusters below 240 K to discrete water clusters around 280 K, a process that leaves the XRD patterns almost unaffected.

2. The second stage, occurring near 340 K, involves the relaxation of these water clusters into a more "flattened" intermediate configuration. This relaxation phase corresponds to a loss of the pillaring effect, leading to a shift of the 002 peak to higher angles and a reversion to the pristine state of MXene. As a result, the sample recovered its conductivity at room temperature.

We also observed an abnormal increase of resistivity between 280 K and 260 K, where $d\rho/dT = -0.7\ \Omega\ cm\ K^{-1}$. This may be due to the disruption of the metallic behavior and inter-flake transport in the MXene/confined water heterostructure due to an increase in turbostratic disorder compared to the pristine structure at a higher temperature (Fig. 3a, d). The constant slope in the metallic region indicates that changes in charge transport occur primarily in the semiconductor-like behavior region (Supplementary Fig. S15). The higher turbostratic disorder may induce a misalignment or twisting of the overlapping MXene flakes that will distort their band structure and, hence, the transport properties of the MXene film[60]. Altering of the electronic properties due to stacking misalignment has already been reported for other 2D materials such as graphene or transition metal dichalcogenides[61,62]. The semiconducting behavior may, therefore, result from a water-driven change in the stacking order of the overlapping MXene flakes in the multilayered film. Electrochemical impedance spectroscopy (EIS) measurements (Supplementary Fig. S21) further support this conclusion by confirming that polarization effects are not dominant in MXene/water heterostructures across the investigated temperature range. The phase angle ($\phi = 0°$) at low frequencies indicates a resistive-dominated response, with no evidence of significant interfacial polarization. This supports the conclusion that the observed semiconductor-like behavior is not caused by polarization but is instead linked to structural changes in confined water and the resulting disruption of MXene stacking order.

This study establishes a direct link between the thermal dependence of electrical resistivity and the structural dynamics of confined water in MXene/water heterostructures. Using temperature-dependent resistivity measurements, in-situ XRD, XPEEM, and DSC, we revealed significant structural transformations of confined water during the first thermal cycle, including interlayer spacing expansion and the formation of amorphous ice clusters. These clusters disrupt the MXene stacking order, driving a metal-to-semiconductor transition in Li^+, Na^+, and K^+ intercalated MXene films. Upon heating above 300 K, the clusters dissociate, restoring the interlayer spacing and metallic behavior. In contrast, H^+ intercalated MXene, lacking confined water, exhibited no such transitions, underscoring the critical role of confined water in influencing electronic properties. In-situ XPEEM provided direct imaging of these water clusters transitioning from amorphous ice to a weakly hydrogen-bonded network upon heating, complementing macroscopic observations from resistivity and XRD. DSC further identified glass transitions associated with the confined water, highlighting its influence on the thermal and structural behavior of MXenes.

While this work provides key insights from the experimental side, further computational studies are needed to fully understand the mechanisms underlying these observations, particularly the role of amorphous ice formation and its impact on electronic transport. Such studies could elucidate atomic-scale interactions between confined water molecules and MXene layers, guiding the design of MXene-based devices where control over interlayer transport, fluid nano-confinement, and phase transitions is essential. In summary, this work highlights the pivotal influence of structural changes and phase transitions in confined water—specifically amorphous ice formation—on the thermal and electronic behavior of MXene films, opening avenues for tailoring their properties for applications in electronics, sensing, and energy storage.

Methods

Materials

For MAX synthesis, TiC (99.5%, −325 mesh), Ti (99.5%, −325 mesh), Al (99.5%, −325 mesh), and graphite (99.0%, −300 mesh) powders were obtained from Alfa Aesar. For MXene synthesis, LiF (Lithium fluoride, Thermo Scientific, 99.85%), HCl (hydrochloric acid, Fisher Scientific, 37 wt%), and deionized water (10–15 MΩ) solutions were used. LiCl (anhydrous, 99%, Thermo Scientific), KCl (potassium chloride, ACS, 99.0% min), and NaCl (sodium chloride, ACS, 99.0% min) were used in intercalation experiments.

MAX phase synthesis

Synthesis of Ti_3AlC_2 MAX followed the procedures reported by Mathis et al.[63]. Specifically, the precursor powders were mixed at a molar ratio of Ti:Al:C = 3.25:2.20:2.00. The precursor powders were mixed in HDPE jars by ball milling for 18 h at ~70 rpm with a 2:1 weight ratio of ZrO_2 balls to powder. The mixed powder was then packed into alumina crucibles, heated under a continuous argon flow (~ 100 sccm) at a rate of 3 °C min^{-1} and held at 1380 °C for 2 hours, then cooled naturally to room temperature. The resulting sintered blocks were milled into fine powders with a TiN-coated milling bit. 50 g powder batches were added to 500 mL of 9 M HCl and stirred overnight to dissolve residual intermetallic species. Then, the MAX phase was collected by vacuum filtration and washed with excess deionized water through a polycarbonate filter membrane (pore size 5 µm). The acid-washed MAX phase was dried in a vacuum oven at 150 °C and sieved through a 400 mesh (38 µm) stainless steel screen to obtain the final powder that was used for the MXene synthesis (<38 µm).

Synthesis of MXene

We prepared a colloidal solution of Li-$Ti_3C_2T_x$ MXene by selectively etching the Al layer from the Ti_3AlC_2 MAX phase using a LiF and HCl mixture[63,64]. Specifically, 1 g of Ti_3AlC_2 powder was reacted with a premixed etchant (1.6 g of LiF and 20 mL of 9 M HCl) for 24 h at room temperature. Then the acid mixture was washed with 150 mL of deionized water for 4-6 cycles until the pH of the supernatant reached a value of 6. Then, the collected sediment was redispersed with 50 mL DI water and hand-shaken for 16 min, followed by centrifugation at 3500 rpm for 10 min to remove unreacted MAX particles and reaction by-products. The dark supernatant was centrifuged at 7500 rpm for 3 min to obtain a solution of single-layer Li-$Ti_3C_2T_x$.

To obtain Na-$Ti_3C_2T_x$ and K-$Ti_3C_2T_x$ and control the solvation shell of water molecules between the MXene layers, Li-$Ti_3C_2T_x$ underwent ion exchange in 5 M KCl and 5 M NaCl solutions. Freestanding films were prepared by vacuum filtration of colloidal solutions with Celgard filter membranes (3501 Coated PP, Celgard, USA). Acid treatment of Li-$Ti_3C_2T_x$ freestanding films was performed to investigate the effect of protons on the properties of MXene/confined water systems. The films were soaked in 3 M HCl to introduce protons into the layers, followed by dip washing with DI water three times to remove excess protons and chlorine from the surface, named as H-$Ti_3C_2T_x$, and dried on a vacuum filter to flatten the film. All samples were stored under vacuum at room temperature for two days before use. To remove the adsorbed confined water, we annealed the samples under high vacuum at 253 K (80 °C) for at least 12 h (<0.01 mbar with a constant vacuum supply).

Thermogravimetric-mass spectrometry analysis

The simultaneous thermogravimetric-mass spectrometry analysis was conducted using a Discovery SDT 650 instrument coupled with a mass spectrometer (TA Instruments, DE). To prepare the samples, vacuum-filtered films of Li^+, Na^+, K^+, and H^+ intercalated $Ti_3C_2T_x$ MXenes were cut into small pieces and packed into a 90 µL alumina pan. The analysis chamber was purged with Ar gas at a flow rate of 300 mL min^{-1} for 1.5 h before heating to remove any residual air. The samples were then subjected to a constant heating rate of 10 °C min^{-1} in an Ar atmosphere (200 mL min^{-1}), with the temperature ramped up to 400 °C for analysis.

Low-temperature electronic transport

The electronic transport properties of freestanding MXene films were measured using a Quantum Design EverCool II Physical Property Measurement System (PPMS). The MXene freestanding film was cut into strips with a rectangular shape of 1 mm × 5 mm and wired to the PPMS sample puck using conductive Ag paint and Ag wire (Supplementary Fig. S19). The temperature-dependent resistance was recorded from 25 °C (300 K) down to −75 °C (200 K) in a low-pressure helium environment (~0.5 Torr). The resistance of each film was recorded while cooling the film from 300 K to 200 K and heating it back at a heating/cooling rate of 3 K min^{-1}. The measurement was repeated for six cooling cycles. At the end of the sixth cycle, heating reached 380 K, and resistivity measurements were taken at a profile of 380 K - 200 K - 380 K.

Synchrotron radiation X-ray diffraction

X-ray diffraction data were obtained using synchrotron radiation at the KMC-2 DIFFRACTION beamline at the BESSY II facility (see Supplementary Fig. S21)[65]. The radiation had an energy of 8.048 keV (corresponding to a wavelength of 1.5406 Å, equivalent to Cu $K\alpha_1$ radiation for rapid comparison with laboratory-based data) and a flux of $f = 10^{11}$ photons s^{-1} mm^{-2}. Diffracted signals were collected over an angular range of 3–39.3° 2θ using a Bruker Vantec 2000 area detector. The 2D diffraction images were azimuthally integrated to obtain 1D diffraction patterns using an in-house program developed at HZB. The samples, cut from MXene sheets, were affixed to a planar sample stage and held at an angle of 45° relative to the incident beam. The low-temperature sample environment, developed in-house at HZB (TMP-CCR-HXR), regulated the temperature through a closed-cycle refrigeration system

and encapsulated the sample stage with two domes. The first dome was evacuated and refilled with helium gas three times prior to measurement to create a low-humidity atmosphere. The measurements were performed with a small amount of helium gas to enhance heat transfer in the central unit. The outer dome was evacuated to a pressure of 10^{-4} mbar to prevent water condensation and freezing when the samples were exposed to low temperatures. Temperatures were measured using a thermocouple within the central unit. Measurements were taken under isothermal conditions at the reported temperatures.

X-ray photoemission electron microscopy

X-ry photoemission electron microscopy (XPEEM) was conducted at the soft X-ray undulator beamline UE49-PGM-A of the BESSY II synchrotron facility[65]. The endstation was equipped with an Elmitec PEEM-III energy microscope/analyzer, allowing energy and spatially resolved imaging. The XA spectra were measured in Partial Electron Yield (PEY) detection mode. The Li-$Ti_3C_2T_x$ MXene sample was prepared by spin coating on a conductive Si substrate and was rapidly transferred under vacuum to a sample holder cooled at 80 K. The temperature was then controlled, and the XPEEM measurements were performed after thermal stabilization. The XAS recorded at the oxygen *K*-edge was fitted using the Multipeak Fitting tool from Igor Pro 8 with Gaussian peaks and an arctangent baseline.

Dimensionality reduction and clustering were performed on XPEEM datasets at the oxygen *K*-edge, for temperatures from 220 K to 300 K, to group pixels with similar spectral behavior. Independent Component Analysis (ICA) was used for dimensionality reduction, excluding the first component to reduce thickness artifacts. A Gaussian Mixture Model (GMM) was then employed to cluster the pixels in the examined MXene region, maintaining a constant number of clusters across different temperatures. Custom Python scripts were utilized for image alignment, interpolation, and clustering[66].

X-ray photoelectron spectroscopy

The X-ray photoelectron spectroscopy (XPS) analysis was conducted on a Physical Electronics VersaProbe 5000 spectrometer (Chanhassen, MN) using a 100 µm monochromatic Al K_α X-ray beam. Photoelectrons were collected at a takeoff angle of 45° between the sample surface and the hemispherical electron energy analyzer. Charge neutralization was achieved using a dual-beam charge neutralizer, which irradiated low-energy electrons and ion beams. Vacuum-filtered films were affixed to carbon tape and electrically grounded using a copper wire. The core-level spectra were deconvoluted and quantified using CasaXPS Version 2.3.16 RP 1.6 software. Before quantification and deconvolution, background contributions to the measured intensities were subtracted using a Shirley function.

Data availability

The temperature-dependent electrical conductivity data are available in Zenodo database under the accession code https://doi.org/10.5281/zenodo.15786192. Further data is available upon request to the authors.

References

1. Dargaville, B. L. & Hutmacher, D. W. Water as the often neglected medium at the interface between materials and biology. *Nat. Commun.* **13**, 4222 (2022).
2. Kolesnikov, A. I. et al. Quantum tunneling of water in beryl: a new state of the water molecule. *Phys. Rev. Lett.* **116**, 167802 (2016).
3. Mallamace, F. et al. The influence of water on protein properties. *J. Chem. Phys.* **141**, 165104 (2014).
4. Monroe, J. et al. Water structure and properties at hydrophilic and hydrophobic surfaces. *Annu. Rev. Chem. Biomol. Eng.* **11**, 523–557 (2020).
5. Raviv, U., Laurat, P. & Klein, J. Fluidity of water confined to subnanometre films. *Nature* **413**, 51–54 (2001).
6. Han, S., Choi, M. Y., Kumar, P. & Stanley, H. E. Phase transitions in confined water nanofilms. *Nat. Phys.* **6**, 685–689 (2010).
7. Alabarse, F. G. et al. Freezing of water confined at the nanoscale. *Phys. Rev. Lett.* **109**, 035701 (2012).
8. Fumagalli, L. et al. Anomalously low dielectric constant of confined water. *Science* **360**, 1339–1342 (2018).
9. Naguib, N. et al. Observation of water confined in nanometer channels of closed carbon nanotubes. *Nano Lett.* **4**, 2237–2243 (2004).
10. Fitzner, M., Sosso, G. C., Cox, S. J. & Michaelides, A. Ice is born in low-mobility regions of supercooled liquid water. *Proc. Natl. Acad. Sci. USA* **116**, 2009–2014 (2019).
11. Artemov, V. G. et al. Anomalously high proton conduction of interfacial water. *J. Phys. Chem. Lett.* **11**, 3623–3628 (2020).
12. Björneholm, O. et al. Water at Interfaces. *Chem. Rev.* **116**, 7698–7726 (2016).
13. Gartner, T. E., Piaggi, P. M., Car, R., Panagiotopoulos, A. Z. & Debenedetti, P. G. Liquid-liquid transition in water from first principles. *Phys. Rev. Lett.* **129**, 255702 (2022).
14. Kaneko, T. et al. Phase behaviors of deeply supercooled bilayer water unseen in bulk water. *Proc. Natl. Acad. Sci. USA* **115**, 4839–4844 (2018).
15. Kapil, V. et al. The first-principles phase diagram of monolayer nanoconfined water. *Nature* **609**, 512–516 (2022).
16. Millot, M. et al. Nanosecond X-ray diffraction of shock-compressed superionic water ice. *Nature* **569**, 251–255 (2019).
17. Neek-Amal, M., Peeters, F. M., Grigorieva, I. V. & Geim, A. K. Commensurability effects in viscosity of nanoconfined water. *ACS Nano* **10**, 3685–3692 (2016).
18. Sugahara, A. et al. Negative dielectric constant of water confined in nanosheets. *Nat. Commun.* **10**, 850 (2019).
19. Simon, P. & Gogotsi, Y. Confined water controls capacitance. *Nat. Mater.* **20**, 1597–1598 (2021).
20. Fleischmann, S. et al. Continuous transition from double-layer to faradaic charge storage in confined electrolytes. *Nat. Energy* **7**, 222–228 (2022).
21. Viger, M. L. et al. Near-infrared-induced heating of confined water in polymeric particles for efficient payload release. *ACS Nano* **8**, 4815–4826 (2014).
22. Bregante, D. T. & Flaherty, D. W. Impact of Specific Interactions among reactive surface intermediates and confined water on epoxidation catalysis and adsorption in Lewis acid zeolites. *ACS Catal.* **9**, 10951–10962 (2019).
23. Boyd, S. et al. Effects of interlayer confinement and hydration on capacitive charge storage in birnessite. *Nat. Mater.* **20**, 1689–1694 (2021).
24. Wang, R. et al. Operando atomic force microscopy reveals mechanics of structural water driven battery-to-pseudocapacitor transition. *ACS Nano* **12**, 6032–6039 (2018).
25. Bell, R. A., Payne, M. C. & Mostofi, A. A. Improving the conductance of carbon nanotube networks through resonant momentum exchange. *Phys. Rev. B Condens Matter Mater. Phys.* **89**, 245426 (2014).
26. Zahab, A., Spina, L. & Poncharal, P. Water-vapor effect on the electrical conductivity of a single-walled carbon nanotube Mat. *Phys. Rev. B* **62**, 10000 (2000).
27. Joshi, R. K. et al. Precise and ultrafast molecular sieving through graphene oxide membranes. *Science* **343**, 752–754 (2014).
28. Osti, N. C. et al. Influence of metal ions intercalation on the vibrational dynamics of water confined between MXene layers. *Phys. Rev. Mater.* **1**, 065406 (2017).
29. Zaman, W. et al. In situ investigation of water on MXene interfaces. *Proc. Natl. Acad. Sci. USA* **118**, 1–9 (2021).

30. Maniwa, Y. et al. Water-filled single-wall carbon nanotubes as molecular nanovalves. *Nat. Mater.* **6**, 135–141 (2007).
31. Sun, Y. et al. Proton redox and transport in MXene-confined water. *ACS Appl. Mater. Interfaces* **12**, 763–770 (2020).
32. Célérier, S. et al. Hydration of $Ti_3C_2T_x$ MXene: an interstratification process with major implications on physical properties. *Chem. Mater.* **31**, 454–461 (2019).
33. Gopinadhan, K. et al. Complete steric exclusion of ions and proton transport through confined monolayer water. *Science* **363**, 145–148 (2019).
34. Gao, Q. et al. Tracking ion intercalation into layered Ti_3C_2 MXene films across length scales. *Energy Environ. Sci.* **13**, 2549–2558 (2020).
35. Chen, H. et al. Pristine titanium carbide MXene films with environmentally stable conductivity and superior mechanical strength. *Adv. Funct. Mater.* **30**, 1906996 (2020).
36. Lounasvuori, M., Zhang, T., Gogotsi, Y. & Petit, T. Tuning the microenvironment of water confined in $Ti_3C_2T_x$ MXene by cation intercalation. *J. Phys. Chem. C.* **128**, 2803–2813 (2024).
37. Hart, J. L. et al. Control of MXenes' electronic properties through termination and intercalation. *Nat. Commun.* **10**, 522 (2019).
38. Maurel, V. et al. Operando AC in-plane impedance spectroscopy of electrodes for energy storage systems. *J. Electrochem. Soc.* **169**, 120510 (2022).
39. Han, M. et al. Electrochemically modulated interaction of MXenes with microwaves. *Nat. Nanotechnol.* **18**, 373–379 (2023).
40. Jiang, J. et al. First-principles molecular dynamics simulations of the spontaneous freezing transition of 2D water in a nano-slit. *J. Am. Chem. Soc.* **143**, 24 (2021).
41. Swenson, J. Possible relations between supercooled and glassy confined water and amorphous bulk ice. *Phys. Chem. Chem. Phys.* **20**, 30095–30103 (2018).
42. Hantanasirisakul, K. et al. Effects of synthesis and processing on optoelectronic properties of titanium carbonitride MXene. *Chem. Mater.* **31**, 2941–2951 (2019).
43. Xu, K., Cao, P. & Heath, J. R. Graphene visualizes the first water adlayers on mica at ambient conditions. *Science* **329**, 1188–1191 (2010).
44. Marcus, Y. Volumes of aqueous hydrogen and hydroxide ions at 0 to 200 °C. *J. Chem. Phys.* **137**, 154501 (2012).
45. Lounasvuori, M. et al. Vibrational signature of hydrated protons confined in MXene interlayers. *Nat. Commun.* **14**, 1322 (2023).
46. Ghidiu, M. & Barsoum, M. W. The {110} reflection in X-ray diffraction of MXene films: misinterpretation and measurement via non-standard orientation. *J. Am. Ceram. Soc.* **100**, 5395–5399 (2017).
47. McKenzie, S. & Kang, H. C. Squeezing water clusters between graphene sheets: energetics, structure, and intermolecular interactions. *Phys. Chem. Chem. Phys.* **16**, 26004–26015 (2014).
48. Hantanasirisakul, K. & Gogotsi, Y. Electronic and optical properties of 2D transition metal carbides and nitrides (MXenes). *Adv. Mater.* **30**, e1804779 (2018).
49. Amann-Winkel, K. et al. Water's second glass transition. *Proc. Natl. Acad. Sci. USA* **110**, 17720–17725 (2013).
50. Melillo, J. H. et al. Complexity of confined water vitrification and its glass transition temperature. *Proc. Natl. Acad. Sci. USA* **121**, e2407030121 (2024).
51. Pylkkänen, T. et al. Role of non-hydrogen-bonded molecules in the oxygen K-edge spectrum of ice. *J. Phys. Chem. B* **114**, 3804–3808 (2010).
52. Nilsson, A. et al. X-ray absorption spectroscopy and X-ray Raman scattering of water and ice; an experimental view. *J. Electron Spectros Relat. Phenom.* **177**, 99–129 (2010).
53. Tang, F. et al. Many-body effects in the X-ray absorption spectra of liquid water. *Proc. Natl. Acad. Sci. USA* **119**, e2201258119 (2022).
54. Wu, B. et al. Water confinement in nitrogen-rich nanoporous carbon materials revealed by in situ scanning transmission X-ray microscopy. *Adv. Funct. Mater.* **34**, 2406528 (2024)
55. Ghidiu, M. et al. Ion-exchange and cation solvation reactions in Ti_3C_2 MXene. *Chem. Mater.* **28**, 3507–3514 (2016).
56. Li, Y., Huang, S., Wei, C., Wu, C. & Mochalin, V. N. Adhesion of two-dimensional titanium carbides (MXenes) and graphene to silicon. *Nat. Commun.* **10**, 3014 (2019).
57. Fang, H. et al. Signatures of band-like optical and charge transport in $Ti_3C_2T_x$ MXene flakes. Preprint at https://doi.org/10.26434/chemrxiv-2024-rpf17 (2024).
58. Rakhmanov, R. et al. Influence of MXene interlayer spacing on the interaction with microwave radiation. *Adv. Funct. Mater.* **35**, 2410591, (2024)
59. Hu, T. et al. Anisotropic electronic conduction in stacked two-dimensional titanium carbide. *Sci. Rep.* **5**, 9525 (2015).
60. Martins, M. L. et al. Water dynamics in pristine and porous $Ti_3C_2T_x$ MXene as probed by quasielastic neutron scattering. *Phys. Rev. Mater.* **6**, 034001 (2022).
61. He, J., Hummer, K. & Franchini, C. Stacking effects on the electronic and optical properties of bilayer transition metal dichalcogenides MoS_2, $MoSe_2$, WS_2, and WSe_2. *Phys. Rev. B* **89**, 075409 (2014).
62. Mak, K. F., Shan, J. & Heinz, T. F. Electronic structure of few-layer graphene: Experimental demonstration of strong dependence on stacking sequence. *Phys. Rev. Lett.* **104**, 176404 (2010).
63. Mathis, T. S. et al. Modified MAX phase synthesis for environmentally stable and highly conductive Ti_3C_2 MXene. *ACS Nano* **15**, 6420–6429 (2021).
64. Schultz, T. et al. Surface termination dependent work function and electronic properties of $Ti_3C_2T_x$ MXene. *Chem. Mater.* **31**, 6590–6597 (2019).
65. Többens, D. M. & Zander, S. KMC-2: an X-ray beamline with dedicated diffraction and XAS endstations at BESSY II. *JLSRF* **2**, A49 (2016).
66. Thevenaz, P., Ruttimann, U. E. & Unser, M. A pyramid approach to subpixel registration based on intensity. *IEEE Trans. Image Process.* **7**, 27–41 (1998).

Acknowledgements

This work was supported by the U.S. Department of Energy (DOE), Office of Science, Office of Basic Energy Sciences, grant No. DE-SC0018618. The authors also acknowledge financial support by DAAD (A.A.), Volkswagen Foundation Freigeist Fellowship 89592 (A.A. and T.P.), European Research Council (ERC) under the European Union's Horizon 2020 research and innovation program, grant 947852 (M.L., F.A., and T.P.). The authors acknowledge the kind support of staff members of the BESSY II synchrotron facility, especially Nico Grimm, Rene Grüneberger, and Dirk Wallacher, for help with the XRD sample environment. The TMP-CCR-HXR sample environment at HZB received funding from the BMBF program ErUM-Pro. We thank HZB for allocating synchrotron radiation beamtimes (proposals 221-11173 EF, 222-11345 EF, 192-08894 EF/R). The authors thank Professor Steve May for helpful discussions on the transport properties of MXene and for providing access to the Physical Property Measurement System (PPMS), Dr. Kanit Hantanasirisakul for initial measurements of temperature-dependent conductivity at Drexel University, and Professor Andre Geim of the University of Manchester for his helpful comments on this work.

Author contributions

T.Z., A.A., R.W., T.P., and Y.G. designed and conducted the experiments. T.Z. and R.W performed the material synthesis and sample preparation. T.Z. performed transport property measurements and XPS analysis. K.A.M., A.A., and M.L. performed the synchrotron XRD measurements with the help of D.T. at BESSY II. R.W. performed the DSC measurements. XPEEM measurements were carried out by A.A, K.A.M., M.A.M., and F.K.

F.A. and K.L. contributed to the data analysis and planning of experiments. T.P. and Y.G. supervised the project.

Competing interests
The authors declare no competing interests.

Additional information
Supplementary information The online version contains supplementary material available at https://doi.org/10.1038/s41467-025-62892-7.

Correspondence and requests for materials should be addressed to Tristan Petit or Yury Gogotsi.

Peer review information *Nature Communications* thanks the anonymous reviewers for their contribution to the peer review of this work. A peer review file is available.